Wavefront curvature sensing on highly segmented telescopes

Gary Chanan

Department of Physics and Astronomy, University of California, Irvine
Irvine, CA 92697

ABSTRACT

Curvature sensing, unlike some other wavefront sensing techniques, treats the boundary and interior of the aperture of interest in fundamentally different ways. This leads to complications for highly segmented telescopes (100 or more segments), as a significant fraction of points on the wavefront are simultaneously in the interior of the overall aperture and near a segment boundary. Although this effect may make it difficult to implement curvature sensing for adaptive optics on such telescopes, it may conversely be exploited for primary mirror segment alignment. We present numerical simulations which show that curvature methods should be an effective method for segment tip/tilt alignment on highly segmented mirrors.

Keywords: telescopes, alignment, astronomical optics

1. INTRODUCTION

Several groups around the world are currently working on the design of extremely large telescopes (ELTs), with highly segmented mirrors, 30 to 100 meters in diameter[1-4]; in virtually all cases, it is assumed that adaptive optics will be an integral part of the telescope. A fundamental issue for these telescopes of the future concerns the type of wavefront sensors to be employed in their adaptive optics and in their mirror alignment systems. [Because the alignment systems for ELTs will have to deal with much larger wavefront errors (but at much lower bandwidth) than the corresponding AO systems, the alignment and AO wavefront sensors will likely be two different devices]. Current AO systems on large telescopes utilize either Shack-Hartmann[5] or curvature wavefront sensors[6], with pyramid wavefront sensors[7-10], currently under development. The adaptive optics systems on the 36-segment Keck telescopes[11-12], and also the (independent) mirror alignment systems on these telescopes[13], provide some experience with Shack-Hartmann sensors on (moderately) segmented mirrors, but curvature sensing on such telescopes in both the AO and alignment contexts remains relatively unexplored. In this paper, we examine some issues associated with curvature sensing on segmented mirrors, especially highly segmented mirrors (~100 or more segments). In Section 2, we briefly discuss the theory of curvature sensing in the context of highly segmented mirrors; in particular we show that the presence in the curvature equation of large boundary terms associated with segment tip/tilt errors may substantially complicate AO wavefront sensing, but conversely that it may facilitate wavefront sensing for segment alignment purposes. In the remainder of the paper we focus on this latter application: In Section 3 we describe a restricted form of curvature sensing, which is only concerned with segment tip/tilt errors and global radius of curvature errors of the primary mirror, and we make rough estimates of its performance. In Section 4, we present Monte Carlo simulations of such wavefront sensing on a 91 segment mirror, such as the Hobby Eberly or Southern African Large Telescope, as well as on a 1080 segment mirror, such as the California Extremely Large Telescope. We show that the algorithm is both accurate and robust. We summarize our conclusions in Section 5.

2. THEORY

In curvature sensing, the curvature – or more precisely the Laplacian – of the wavefront is obtained from out of focus images of a star. The fundamental equation of curvature sensing[14-16] is:

$$\frac{I_+ - I_-}{I_+ + I_-} = \frac{f(f-L)}{L}\left(\delta_r \frac{\partial \varphi}{\partial r} - \nabla^2 \varphi\right) \qquad [1]$$

where I_- and I_+ are the intensities at a point in the image inside and outside of the focus, f is the focal length, L is the extra-focal distance, φ is the phase (in units of length, not angle), $\partial\varphi/\partial r$ is the derivative normal to the boundary, δ_r is the delta function centered at the boundary, and ∇^2 is the Laplacian operator. Note that the derivatives are with respect to the coordinates of the primary mirror (not the coordinates of the image on the detector). We refer to the pixel-by-pixel ensemble of values on the left hand side of Eq. 1 as the (normalized) difference image.

Because of the delta function, the first derivative does not contribute to the curvature signal in the interior of the pupil, but it does contribute near the boundary. Here, in practice, "near" means within one resolution element of the boundary. Let us integrate Eq. 1 over a boundary resolution element, where the size of this element, referred to the primary, is p; we assume that $\nabla^2\varphi$ varies only slowly over p. The integral of the derivative terms in Eq. 1, which we abbreviate as S, is then approximately:

$$S = \frac{\partial \varphi}{\partial r} - p\nabla^2 \varphi \qquad [2]$$

The resolution element may be one pixel on the detector (in an AO corrected image) or the size of the seeing disk in an uncorrected image. If there are n resolution elements across the pupil (in one dimension), then $p = D/n$, where in general we expect $n >> 1$ for a high order wavefront sensor.

We can estimate S in Eq. 2 by making approximations such as $\partial\varphi / \partial r \sim \varphi_{rms} / R$, where R is the radius of the primary mirror; thus:

$$S \sim \frac{\varphi_{rms}}{R} - \frac{p\varphi_{rms}}{R^2} \qquad [3]$$

The ratio of the second term to the first term is thus $2/n$, which is in general a small number. Thus for most pixels in the difference image formed by a monolithic mirror we only need to consider one or the other of the derivative terms in Eq.1: In the interior, the first derivative is absent; near the boundary, the first derivative is dominant and the second derivative can generally be ignored. It is possible in principle to extract information on both derivatives from a boundary pixel, but this is difficult in the presence of noise, because the contribution due to the second derivative is only a small fraction of that due to the first derivative.

Note that curvature sensing mixes different order terms in the same pixel: a first order term due to the wavefront curvature and a zeroth order term due to the first derivative near a boundary (where in general the left hand side of Eq. 1 will be +/-1). [By contrast, for a Shack-Hartmann or a pyramid sensor, each pixel contains only gradient information and there is no mixing of orders.]

The above analysis assumed a monolithic mirror. Suppose instead that we have a highly segmented mirror. Let the segment radius (or hexagon side length) be a, so that $R^2/a^2 \approx N$, where N is the total number of segments in the mirror. Let $m = a/p$ be the number of resolution elements across the contribution of the defocused image due to an individual segment; we might have $m < 1$ (unresolved segments) or $m > 1$ (resolved segments). For the moment, we

consider the marginal case of $m = 1$. In this case virtually every pixel contains contributions both from first derivatives at the segment boundaries and second derivatives from global mirror aberrations evaluated in the interior. The sizes of the two corresponding contributions to the intensity in the difference image are $\varphi_{segment}/a^2$ and φ_{global}/R^2 respectively. Thus, for a highly segmented telescope with $N \sim 1000$, a few nanometers of segment aberrations will provide an effective background of a few *microns* against which global aberrations must be measured. [To set the scale, note that all of the terms in the proposed adaptive optics error budget for the California Extremely Large Telescope[17] add up to about 100 nm.] Clearly, the situation is even worse for $m < 1$.

To avoid these high effective backgrounds, we can move to the resolved case where $m > 1$. This potentially gets around the background problem because we can then sort pixels according to whether or not they contain boundary contributions; we simply look for global aberration information in those pixels which are uncontaminated by segment boundary effects. However, there is another problem with operating in this regime, as shown in the following.

At a point in the interior of the image, the difference ΔI between either I_+ and I_- (defined as above) and the corresponding intensity I for an aberration-free (but still out-of-focus) image satisfies:

$$\frac{\Delta I}{I} = \pm \frac{f(f-L)}{L} \nabla^2 \varphi \qquad [4]$$

We neglect L compared to f, estimate $\nabla^2\varphi$ as above, introduce $D = 2R$ as the full primary mirror diameter, and relate L to the overall out-of-focus image size $\Delta\theta$ (in arcseconds) by simple geometrical optics:

$$L = \frac{f^2 \Delta\theta}{206265\ D} \qquad [5]$$

to obtain:

$$\frac{\Delta I}{I} = 0.8 \frac{\varphi_{rms}}{D\ \Delta\theta} \qquad [6]$$

where φ_{rms} is in microns. Thus both the large diameter of the telescope and the desire to resolve segments in the out-of-focus image work to reduce $\Delta I/I$ and hence the strength of the curvature signal. Consider the California Extremely Large Telescope, which as currently planned will have 1080 hexagonal segments 0.5 meters on a side, for a total diameter of 30 meters. If we assume that resolving segments will require at least one arcsecond per segment in the defocused image, then this image will subtend at least 35 arcseconds. For $\varphi_{\rm rms} = 1$ micron, we then find $\Delta I/I \leq 0.0008$, which is a discouragingly small curvature signal.

Of course the argument that AO-type curvature sensing on highly segmented telescopes must contend with large intrinsic backgrounds or small signals does not constitute a proof that this technique is unworkable. It does, however, point to significant challenges to the implementation of AO curvature sensing on ELTs - particularly in the area of closing the control loop - that simply do not apply to "pure gradient" methods, such as Shack-Hartmann or pyramid sensing. In any case, we shall not consider curvature sensing for AO on ELTs any further in the present work. Conversely, however, the large segment boundary effect suggests that out-of-focus images may provide useful data on segment alignment. We explore this in the following section.

3. A MODIFIED CURVATURE SENSING APPROACH TO SEGMENT ALIGNMENT

Here we consider a modification of curvature sensing designed to solve the restricted wavefront sensing problem of determining segment tip/tilts, and (as we shall show) the related problem of determining the primary mirror global radius of curvature. We assume that diffraction effects may be neglected because of seeing (in the long exposure limit) and also because we will ultimately average over a reasonably large wavelength interval. Thus the technique involves only

geometrical optics and is therefore blind to such effects as segment piston errors. Techniques for diagnosing piston errors in ELTs have been discussed elsewhere.[18-19]

In the geometrical optics regime, it is easy to describe the effect of low order segment aberrations on the out-of-focus image without reference to the basic differential equation [Eq. 1]. A tip or tilt will simply displace the subimage associated with the segment as a rigid body in the out-of-focus image plane. [In the geometrical optics limit and in the absence of seeing, this subimage has the same shape as the segment itself.] A focus error will expand or contract the subimage radially, with a corresponding decrease or increase, respectively, in the subimage brightness. An astigmatic error will expand the subimage in one direction and contract it in the orthogonal direction, without changing its (uniform) brightness. The simulated images generated in the Monte Carlo study discussed in Section 4 were generated using an algorithm based on these simple rules.

In this section, we reverse the point of view in Section 2: there, segment boundary effects were regarded as a background against which continuous global aberrations had to be determined; here, the former effects are the signal, and the latter constitute the noise. To make this quantitative, imagine an initially perfect primary in which one segment is tipped so that the subimage it creates moves by an angle α in the image plane. Let r be the angular size of a resolution element on the detector; typically in the absence of AO the resolution element is the seeing disk and $r \approx 1$ arcsecond. For $\alpha = 0.01$ arcseconds, the resulting intensity variation in the out-of-focus image (not the difference image) is $\alpha/r \sim 0.01$, or a full order of magnitude larger than that associated with a (global) phase error of 1 micron, as estimated in Section 2.

We also expect that out-of-focus images are sensitive to global radius of curvature errors. Such errors (in which the central rays from all segments intersect at a single point which does not lie in the focal plane of the individual segments) are particularly important for segmented telescopes, as this degree of freedom is generally the most poorly controlled of all primary mirror degrees of freedom.[20] Normal telescope focusing procedures generally insure that radius of curvature errors are accompanied by an almost compensating despace of the secondary mirror. However, the aberrations are not quite degenerate; the net effect is to produce a common focus error on all segments. These focus errors produce slope discontinuities at all of the intersegment edges, and by an argument similar to those given above, these should also produce large effects in the out-of-focus images.

To investigate these ideas more systematically we have written a Monte Carlo code to generate and then extract misalignment errors (both segment tip/tilt and global radius of curvature) for highly segmented telescopes, as described in the following section. We do this both in the context of 100 segment telescopes and 1000 segment telescopes.

4. MONTE CARLO SIMULATIONS

4.1. Description of the Algorithm

For definiteness, we initially consider the restricted curvature sensing algorithm in the context of a 91 segment geometry, arranged in five hexagonal rings. Nominally there are two tip/tilt degrees of freedom for each segment (as noted earlier, piston errors are not observable with this algorithm), plus what we shall refer to as "differential focus mode" for a total of 183 modes. By the latter mode, we mean the global radius of curvature distortion of the primary *plus* the compensating despace of the secondary mirror, so that the net effect is (exactly) an identical focus error in each individual segment; this net aberration can therefore not be expressed as a linear combination of segment tip/tilts alone. The 91 segments have 240 intersegment edges plus 66 peripheral edges. All 306 edges contain information on the aberrations of interest. However, the analysis of the outer or peripheral edges involves some subtleties. In particular, a required rescaling of the images (see discussion of errors below) will strongly affect the measurement of differential focus mode if the peripheral edges are utilized, but not if they are ignored. Therefore, for simplicity we will ignore the peripheral edges and only consider analysis of the 240 intersegment edges for the remainder of this work.

There is, however, a price to be paid for ignoring the peripheral edges. Analysis of the "control matrix," which relates the edge measurements to the misalignments of interest, shows that there are no singular modes when the peripheral edges are utilized, but four modes are singular or nearly singular when they are ignored. [There is also a small decrease in sensitivity when the peripheral edges are ignored which is simply associated with the reduction in the number of

independent measurements.] Three of these four singular modes can be shown to be global tip and tilt and global (not differential) focus mode. In the latter mode (which is only approximately singular), each segment is tilted radially according to:

$$\alpha_x(i) = c_f x_c(i)$$
$$\alpha_y(i) = c_f y_c(i) \qquad [7]$$

where $\alpha_x(i)$ is the x-component of image tilt associated with the ith segment, $x_c(i)$ is the x-coordinate of the center of the ith segment, and similarly for y; c_f is the focus-mode constant of proportionality, which is the same for x and y. [There is no compensating despace of the secondary.] The loss of global tip/tilt information is inconsequential (these are just pointing errors), and the loss of global radius of curvature is not a problem, since sensitivity to differential focus mode is retained. However, the fourth singular mode is "curl," in which each segment is tilted azimuthally according to:

$$\alpha_x(i) = -c_c y_c(i)$$
$$\alpha_y(i) = +c_c x_c(i) \qquad [8]$$

where c_c is the curl mode constant of proportionality for both x and y. This mode manifests itself as a rotation of the out-of-focus images, in opposite directions for inside- and outside-of-focus. Measurement of this "missing mode" ultimately needs to be addressed, perhaps by a sequential technique in which, for example, one looks at the peripheral edges after radius of curvature errors are adequately corrected, but we ignore such details for the purposes of the present discussion.

To return to the Monte Carlo calculation, we first define a standard position on the detector (e.g. the exact center) and a standard out-of-focus distance; this in turn defines standard positions (pixel coordinates) for the locations of each of the intersegment edges in the out-of-focus images. Simulated images for arbitrary configurations of the primary mirror are generated using the simple rules defined in Section 3. The inside-of-focus image is rotated 180 degrees about the optic axis before subtraction, so that a given ray hits the same pixel in both the inside- and outside-of-focus images. The two images are normalized so that they both contain the same total number of counts. We sum the intensity over all pixels in a small box, typically about 2 arcsec on a side, at the location of each intersegment edge in the difference image. [The resulting signal may be either positive or negative.] To determine the correspondence between these edge signals and the x-tilt of the associated segment, we deliberately (in software) tilt a standard interior segment by a standard amount (e.g. 0.05 arcsec) and measure the resulting signal in the six surrounding edges. The same procedure is repeated for y-tilt. We assume that the relationship between tilt and signal is the same for all segments. Finally, we introduce a standard amount (e.g. 200 nm) of Zernike focus error on each segment and measure the resulting edge signal averaged over all edges.

Once we have the relationship between a given tilt and the corresponding edge signal (and similarly for segment defocus) we can extract all of the relevant information from a difference image by assuming that the process is linear and solving the resulting system of 240 equations in 183 – 4 = 179 unknowns. We do this by constructing the pseudo-inverse of this "control matrix" by means of singular value decomposition[21]. This technique not only finds the best solution to the problem in a least squares sense, but at the same time diagnoses the singular and nearly singular modes, which in this case are not all obvious, in particular the curl mode described above. Because the algorithm is not strictly linear (see following discussion of errors), it must be applied iteratively, but, as the Monte Carlo results show, the convergence is reasonably rapid.

4.2. Sources of Error

We consider five different sources of error for the algorithm: non-linearities, shifting/rescaling effects, "template errors" which reflect uncertainties in the value of r_0 used to produce the template images, counting statistics, and segment aberrations.

4.2.1 Non-Linearities

The linear hypothesis – that a given edge signal is directly proportional to the tilt of the associated segment - is true in the limit of small tilts and highly defocused images, but in the presence of large tilts and/or seeing this will not be exactly true: a fraction of the edge signal will spill out of the defining box, and this fraction will vary with the amount

of tilt. This non-linearity can be minimized by increasing the defocus distance, but even in the case when the non-linearity is significant, the algorithm will still converge (although not in a single step), as long as the tilts are within a reasonably well-defined capture range. The capture range will depend on the defocus distance and the tip/tilt values used in construction of the templates. A full treatment is beyond the scope of this work, but we note that in general there is an inverse relation between capture range and accuracy.

4.2.2 Shifting and Rescaling Errors

For proper extraction of the edge signals, the out-of-focus images must be properly registered with respect to the center of the CCD and also at the correct defocus distance. In general one cannot count on the pointing/tracking of the telescope nor on the defocus mechanism to insure that these conditions are met to a high degree of accuracy. Rather, the images must be appropriately shifted and rescaled after the fact in software. Here we simply assert that, with sub-pixel interpolation, this image processing can be done to the required accuracy. We demonstrate this by introducing deliberate translation and scale errors in the images generated in our simulations and then blindly compensating for them with a simple shift-and-rescale algorithm (not described here).

4.2.3 Template Errors

As described above, the modified curvature sensing algorithm requires the generation of templates for tip, tilt, and segment focus errors. The actual signals are extracted by comparing the difference image intensities at the various intersegment edges to the templates. Realistic templates must include the effects of seeing; however, this gives rise to errors, since in general the value of the coherence diameter r_0 used in the template will not precisely match the value of r_0 for the actual images. We include errors of this type in our Monte Carlo simulations by introducing a deliberate error in the value of r_0 used to prepare the templates, compared to the value in the simulated images. Since the exposures are expected to be long (of order 60 seconds) because of the large extra-focal distance, we assume that the atmosphere is sufficiently well described by the long exposure limit.

4.2.4 Counting Statistics

It is clear that this algorithm requires highly defocused images. In particular, for the intersegment edges in the pupil to map unambiguously to the defocused image, the image diameter θ_d must be a factor of several larger than $\sqrt{N}\,\theta_{\rm res}$ where N is the total number of segments in the primary mirror and $\theta_{\rm res}$ is the size of a resolution element, typically the size of the seeing disk. Empirically, we find that the performance begins to fall apart when the ratio $\rho = \theta_{\rm d} / (\sqrt{N}\,\theta_{\rm res})$ is $\lesssim 2$; therefore in our simulations we take this ratio to be several times larger than this. For the five ring mirror, with $N = 91$, we take the overall defocused images to be one arcminute across. For CELT, with $N = 1080$, we take the images to be two arcminutes across. The corresponding ρ values are about 6 and 4, respectively.

For such highly defocused images, photon counting statistics are a concern. Let us consider a target star with V = 8. A star with V = 0 delivers 3.75×10^{-9} ergs cm^{-2} s^{-1} A^{-1} at λ = 5500 Angstroms to the top of the earth's atmosphere[22]. Therefore assuming V = 8, a bandwidth of 1000 Angstroms, an integration time of 30 seconds, an overall throughput of 10%, an aperture diameter of 10 meters, an image diameter of 60", and a box size of 2 arcseconds by 2 arcseconds at each intersegment edge, we find 10^6 photons per edge in the defocused image. As long as we take the defocus distance to be proportional to the number of segments across the primary mirror diameter, this result will be roughly independent of the number of segments. Thus for 8th magnitude stars, counting statistics will give rise to errors of about 1 part in 1000 in the measurement of the edge signals of interest; these errors are small compared to those associated with the intrinsic non-linearities of the algorithm (but we include them anyway in the simulations).

4.2.5 Segment Aberrations

We argued above that smooth global aberrations of the telescope wavefront produce only small perturbations in the difference images compared to the effects of individual segment tip/tilt errors. Simply stated, the local segment effects are multiplied by a factor of R^2/a^2, where R and a are the primary mirror and segment radii, respectively. However, higher order segment aberrations, such as astigmatism and focus, suffer a similar amplification, and such aberrations therefore are far more likely than global ones to limit the sensitivity of this alignment tool. We might guess that the rms amplitude of the higher order segment aberrations themselves provides an estimate (to within a factor of order unity) of

the contributions to the wavefront error from residual misalignments resulting from this effect. The simulations below show that this is indeed the case.

4.6 Results

We have performed Monte Carlo simulations for the restricted curvature sensing algorithm for three different cases in the five ring geometry. In all three cases the defocused images are 60 arcseconds in diameter. The image scale is 0.1 arcseconds per pixel and the boxes over which the edge signals are integrated are 1.9 arcseconds on a side. The overall CCD is 1024 pixels on a side.

The initial conditions involve tip/tilt errors of about 0.3 arcseconds (one dimensional rms, measured on the sky) and segment focus errors of 200 nm (measured at the wavefront, not at the glass surface). The tip/tilt errors exclude the four singular degrees of freedom as discussed above. The three cases are progressively more realistic, in order to give an idea of the relative sizes of the effects of various error sources. Case 1 includes the effects of shifting and rescaling the images, but no seeing or other sources of error are included. The shift errors were 0.5 arcseconds in each dimension, and the scale errors were 0.5%. Case 2 adds seeing and its associated non-linearities, plus template errors and photon statistics errors. The template errors were equivalent to an error of 20% (fixed) in the estimation of r_0. The seeing was assumed to be 1 arcsecond at 0.5 microns, which scales to 0.94 arcseconds at the assumed observing wavelength of 0.7 microns. Photon statistical errors were 0.1% (rms) on each edge signal, as estimated above. Case 3 includes all of the above error sources plus segment aberrations, in particular 20 nm (rms) each of the Zernike focus and the two astigmatism terms, for a total equivalent rms error of 34 nm.

We have also performed the analogous simulations (Cases 4, 5, and 6) for the CELT geometry. Here, the defocused images are 120 arcseconds in diameter and the seeing, when it is included, is taken to be 1 arcsecond at 0.5 microns, as before. In this case the CCD is 2048 pixels on a side. Parameters for all six cases are summarized in Table 1.

Table 1. Parameters for Various Monte Carlo Runs

	Case 1	Case 2	Case 3	Case 4	Case 5	Case 6
Geometry	5 ring	5 ring	5 ring	CELT	CELT	CELT
Pixel Size	0.1"	0.1"	0.1"	0.1"	0.1"	0.1"
CCD Size	1024	1024	1024	2048	2048	2048
Image Size	60"	60"	60"	120"	120"	120"
Shift and Rescale	yes	yes	yes	yes	yes	yes
Seeing	no	yes	yes	no	yes	yes
Template Errors	no	yes	yes	no	yes	yes
Photon Statistics	no	yes	yes	no	yes	yes
Segment Aberrations	0	0	34 nm	0	0	34 nm

Table 2. Monte Carlo Results

		Case 1	Case 2	Case 3	Case 4	Case 5	Case 6
Tip/Tilt Error	Initial	0.281"	0.281"	0.281"	0.277"	0.277"	0.277"
	Iteration 1	0.025"	0.046"	0.055"	0.083"	0.103"	0.103"
	Iteration 2	<0.001"	0.005"	0.025"	0.023"	0.045"	0.057"
	Iteration 3	<0.001"	0.001"	0.031"	0.006"	0.021"	0.040"
Focus Error	Initial	0.200 μ	0.200 μ	0.200 μ	0.200 μ	0.200 μ	0.200 μ
	Iteration 1	0.019 μ	0.036 μ	0.020 μ	0.066 μ	0.050 μ	0.039 μ
	Iteration 2	0.001 μ	0.003 μ	0.010 μ	0.008 μ	0.001 μ	0.010 μ
	Iteration 3	0.002 μ	0.001 μ	0.012 μ	0.005 μ	0.010 μ	0.009 μ

Table 2 gives the results of the simulations for tip/tilt and focus errors before and after each iteration. Figure 1(a) (5 ring geometry) shows the initial one-sided image corresponding to Case 2; Figure 1(b) shows the corresponding image after one iteration and Figure 1(c) after three iterations. Figures 2(a), 2(b), and 2(c) (CELT geometry) show the analogous results corresponding to Case 5. The results for Cases 1, 2, 4, and 5 show that the algorithm is robust with respect to pointing and focus errors, seeing, template errors, and photon statistics. The principal limitation does not come from any of these effects, but rather from segment aberrations. In both Cases 3 and 6 the tip/tilt correction converges rapidly to the point where the rms wavefront errors associated with tip/tilt (expressed in microns) are comparable to the rms wavefront errors due to all other segment aberrations. We would not expect many applications where it is important to have the tip/tilt wavefront errors much smaller than those due to higher order aberrations.

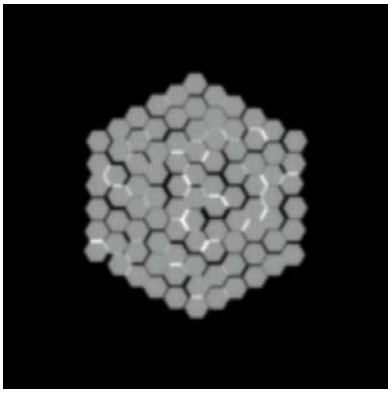

Figure 1(a)

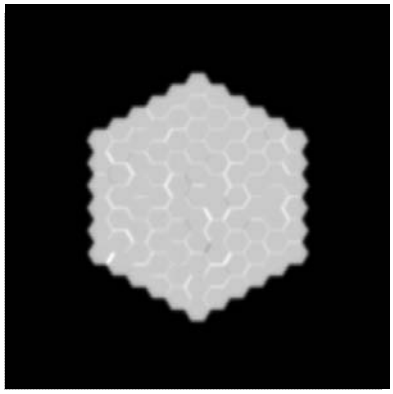

Figure 1(b)

Figure 1(c)

Figure 1(a): Initial one-sided out-of-focus image corresponding to Case 2 for the 5 ring, 91 segment geometry. Segment tip/tilt errors are manifested as shifts in the "segment" positions; global radius of curvature error causes uniform gaps or overlaps. Figure 1(b): Same as 1(a), but after one iteration of the algorithm. Figure 1(c): Same as 1(b), but after three iterations.

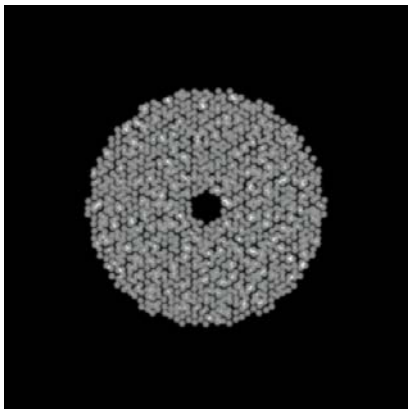

Figure 2(a)

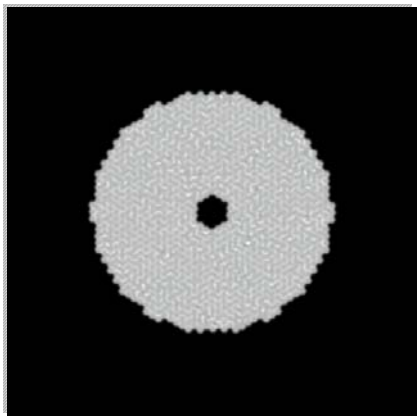

Figure 2(b)

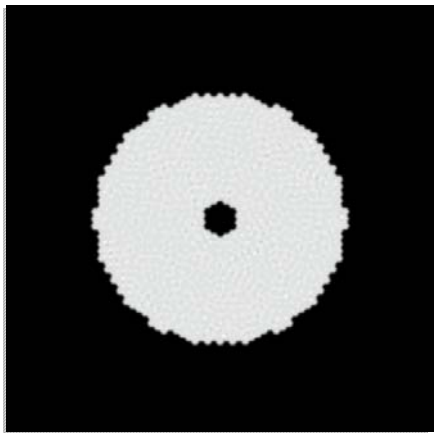

Figure 2(c).

Figure 2(a): Initial one-sided out-of-focus image corresponding to Case 5 for the 1080 segment CELT geometry. Segment tip/tilt errors are manifested as shifts in the "segment" positions; global radius of curvature error causes uniform gaps or overlaps. Figure 2(b): Same as 2(a), but after one iteration of the algorithm. Figure 2(c): Same as 2(b), but after three iterations.

The slower convergence and larger asymptotic errors for the CELT simulations compared to those for the 5 ring geometry do not necessarily have any fundamental significance, but rather may simply reflect the fact that the algorithms have not been optimized and that the chosen CELT defocus distance was proportionally smaller than that used in the 5 ring simulations. Analysis of the respective control matrices in Cases 1 and 4 shows that the corresponding error multipliers (the ratio of rms tip/tilt errors to rms curvature signal errors) are within a few percent of one another, so that the performance should not degrade as the number of degrees of freedom increases.

The focus mode performance, also limited by segment aberrations, is about 10 nm of wavefront error for both geometries. Although this number is not necessarily negligible, it nevertheless probably represents an acceptable

contribution to an overall wavefront error budget, especially for what is likely to be the most poorly controlled primary mirror mode. The situation is less clear in the event that there are other constraints (besides its direct contribution to the overall wavefront error) on the global radius of curvature. For example, the design of the prime focus corrector for the Hobby Eberly Telescope places a very tight tolerance on this parameter[23]. [There is no corresponding effect for CELT, which is not planned to be used at prime focus.] The global radius of curvature tolerance δR_c can be related to the corresponding tolerance on the mean segment (wavefront) Zernike focus coefficient by:

$$\delta R_C = 8\frac{f^2}{a^2}\,\delta C_{20} \qquad [9]$$

The above segment value of δC_{20} = 10 nm corresponds to a global radius of curvature error of about 75 microns for HET, which is a factor of several larger than the very tight design tolerance on this quantity. It is worth noting, however, that virtually any wavefront sensing scheme will have to contend with the very large error-multiplying coefficient - of order 10^4 to 10^5 - on the right hand side of Eq. (9).

5. CONCLUSIONS

For curvature sensing on highly segmented mirrors, we have shown that zeroth order effects associated with segment tip/tilt errors tend to overwhelm the (first order) curvature signal unless the image is so far out of focus that individual segments can be resolved. This constraint may make it difficult to do curvature sensing for adaptive optics on highly segmented telescopes, but this phenomenon can conversely be exploited as the basis of a robust technique for aligning the segments in tip/tilt as well as in focus mode or global radius of curvature. The alignment algorithm described here is only approximately linear and hence must be used iteratively. Nevertheless it converges rapidly and is reasonably robust with respect to errors associated with image processing effects, seeing, and counting statistics. The principal limitation is probably due to segment aberrations; in the presence of such aberrations, the residual misalignments, expressed as an overall wavefront error, will be about the same size as the segment aberrations themselves.

6. ACKNOWLEDGMENTS

I am grateful to Matthias Schoeck and Lothar Noethe for helpful comments on the manuscript. This work has been supported in part by the National Science Foundation Science and Technology Center for Adaptive Optics, managed by the University of California at Santa Cruz under cooperative agreement No. AST-9876783.

7. REFERENCES

1. J.E. Nelson, in "Telescope Structures, Enclosures, Controls, Assembly/Integration/Validation, and Commissioning", T.A. Sebring and T. Anderson, eds., Proc. SPIE, 4004, 282-289 (2000).
2. P. Dierickx and R. Gilmozzi, in "Telescope Structures, Enclosures, Controls, Assembly/Integration/Validation, and Commissioning", T.A. Sebring and T. Anderson, eds., Proc. SPIE, 4004, 290-299 (2000).
3. T. Anderson, A. Ardeberg, J.M. Beckers, R. Flicker, N.C. Jessen, A. Gintcharov, E. Manning, M. Owner-Petersen, and M. Riewaldt, Proc. "ESO/Lund University Backaskog Workshop on Extrememly Large Telescopes" (1999).
4. F.N. Bash, T.A. Sebring, F.B. Ray, and L.W. Ramsey, Proc. SPIE, 2871, 576-584 (1997).
5. R. Shack and B. Platt, JOSA, 61, 656 (1971).
6. F. Roddier et al. PASP, 103, 131-149 (1991).
7. Pugh, W.N., Lobb, D.R. Walker, D.D. and Williams, T.L., in "Adaptive Optical Systems and Applications", ed. R.K. Tyson and R.Q. Fugate, Proc. SPIE, 2534, 312 (1995).
8. Ragazzoni, R., J. Mod. Optics, 43, 289 (1996).
9. Ragazzoni, R. and Farinato, J., Astron. Astrophys, 350, L23 (1999).
10. Riccardi, A., Bindi, N., Ragazzoni, R., Esposito, S., and Stefanini, P., in "Adaptive Optical System Technologies", ed. D. Bonaccini and R.K. Tyson, Proc. SPIE, 3353, 758 (1998).

11. Wizinowich, P., Acton, D.S., Shelton, C., Stomski, P., Gathright, J., Ho, K., Lupton, W., Tsubota, K., Lai, O., Max, C.E., Brase, J., An, J., Avicola, K., Olivier, S., Gavel, D., Macintosh, B., Ghez, A., and Larkin, J., PASP, 112, 315 (2000).
12. Wizinowich, P., Acton, S., Gregory, T., C., Stomski, P.J., An, J.R., Avicola, K., Brase, J.M., Friedman, H.W., Gavel, D.T., and Max, C.E., in "Adaptive Optical System Technologies", ed. D. Bonaccini and R.K. Tyson, Proc. SPIE, 3353, 568 (1998).
13. G.A. Chanan, J. Nelson, T. Mast, P. Wizinowich and B. Schaefer, in "Instrumentation in Astronomy VIII", D.L.Crawford and E.R. Craine, eds., Proc. SPIE, 2198, 1139-1150 (1994).
14. Roddier, F., Appl. Optics, 27, 1223 (1988).
15. Roddier, F., Appl. Optics, 29, 1402 (1990).
16. Roddier, N., in "Active and Adaptive Optical Systems", ed. M.A. Ealey, Proc. SPIE, 1542, 120 (1991).
17. J.E. Nelson, et. al. CELT Greenbook, Vol. 1 (2002).
18. G. Chanan, J. Nelson, C. Ohara, and E. Sirko, in "Telescope Structures, Enclosures, Controls, Assembly/Integration/Validation, and Commissioning", T.A. Sebring and T. Anderson, eds, Proc. SPIE, 4004, 363-372 (2000).
19. G. Chanan, C. Ohara, and M. Troy, Applied Optics, 39, 4706-4714 (2000).
20. M. Troy, G. Chanan, E. Sirko, and E. Leffert, in "Advanced Technology Optical/ I.R. Telescopes VI", Proc. SPIE, 3352, 307-317 (1998).
21. W. Press, B. Flannery, S. Teukolsky, and W. Vetterling, *Numerical Recipes: The Art of Scientific Computing*
(Cambridge University Press: New York), 484-487 (1989).
22. J.S. Drilling and A.U. Landolt, in *Allen's Astrophysical Quantities*, A.N. Cox, ed., (Springer-Verlag: New York), 381-382, (2000).
23. J. Booth, McDonald Observatory, University of Texas at Austin, Austin, TX 78712 (personal communication, 2001).